

Torsional Oscillations in a Global Solar Dynamo

Solar Physics

P. Beaudoin¹ · P. Charbonneau¹ ·
E. Racine² · P.K. Smolarkiewicz³ ·
M. Ghizaru¹

© Springer ●●●

Abstract We characterize and analyze rotational torsional oscillations developing in a large-eddy magnetohydrodynamical simulation of solar convection (Ghizaru, Charbonneau, and Smolarkiewicz, 2010; Racine *et al.*, 2011; Charbonneau and Smolarkiewicz, 2012) producing an axisymmetric large-scale magnetic field undergoing periodic polarity reversals. Motivated by the many solar-like features exhibited by these oscillations, we carry out an analysis of the large-scale zonal dynamics, separating the contributions arising from large-scale flows and magnetic field, namely magnetic torques and Coriolis force acting on the meridional flow, and small-scale contributions associated with Reynolds and Maxwell stresses. Through an analysis of the associated angular momentum fluxes, we demonstrate that torsional oscillations are not driven primarily by the periodically-varying large-scale magnetic torque, as one might have expected, but rather via the magnetic modulation of angular momentum transport by the large-scale meridional flow. This surprising result is confirmed by a simple energy analysis, which indicates that globally and in a time-average sense, only the Coriolis term drives a net input of energy into the mean zonal flow. We also examine the dynamical nature of the rotational coupling existing between the convection zone and underlying stably stratified fluid layers, and find a fairly sharp transition in rotational dynamics taking place as one moves from the base of the convecting layers to the base of the thin tachocline-like shear layer forming immediately below. We conclude by discussing the implication of our analyses with regards to the mechanism of amplitude saturation in the global dynamo operating in the simulation, and speculations on the possible precursor value of torsional oscillations for the forecast of solar cycle characteristics.

Keywords: Sun : torsional oscillations, magnetohydrodynamics, simulation

¹ Département de Physique, Université de Montréal

emails :

beaudoin@astro.umontreal.ca ; paulchar@astro.umontreal.ca

mihai@astro.umontreal.ca

² Canadian Space Agency

³ National Center for Atmospheric Research, Boulder, CO
80307-3000

1. Introduction

Differential rotation of the solar surface was first noted in the seventeenth century by Christoph Scheiner on the basis of his extensive sunspot observations. In his 1632 *Rosa Ursina*, Scheiner states that sunspots moved more slowly the farther away they were from the solar equator, and even concludes that “...From this phenomenon is drawn the strongest argument for a fluid surface of the Sun.” (*Rosa Ursina*, p. 559; as cited and translated in Mitchell, 1916, p. 440). Rediscovered in the mid-nineteenth century by R.C. Carrington and G. Spörer and soon thereafter extended to high latitudes by Doppler measurements, solar differential rotation has now been mapped deep into the Sun by helioseismology (Christensen-Dalsgaard, 2002; Howe, 2009). From the frequency splitting of acoustic eigenmodes of varying azimuthal orders, it has now been shown that the surface latitudinal differential rotation pattern, with the solar equator rotating approximately 30% faster than the poles, persists throughout the bulk of the solar convective envelope, down to $r/R \simeq 0.71$, where it abruptly vanished across a thin spherical shear layer located immediately beneath the core-envelope interface, known as the tachocline. The underlying stably-stratified core appears to be rotating rigidly (or nearly so) down to $r/R \simeq 0.3$, at a rate equal to that of the surface mid-latitudes (see, e.g., Howe, 2009, and references therein).

This internal differential rotation pattern has remained generally steady since the first helioseismic rotational inversions carried out in the late 1980’s; but not *exactly* steady. Rotational torsional oscillations were first noted in surface Doppler measurements (Howard and Labonte, 1980), and later shown by helioseismology to extend all the way to the base of the Sun’s convective envelope. The torsional oscillation signal only reaches a few nHz in amplitude (about 0.5% of the rotational frequency), and peaks at high latitudes and in surface and subsurface layers. The oscillations develop at twice the solar cycle frequency and, at mid- to high latitudes (where the signal is the strongest), retains the same phase at all depths (see, e.g., Fig. 26 in Howe, 2009). More elaborate phasing patterns occur with latitudes with two diverging “branches” of faster rotating fluid appearing at mid-latitudes around solar activity minimum : one migrating all the way down to the equator in the span of two full activity cycles, the other migrating poleward to cause a marked spin-up of the polar region peaking at around the time of activity maximum (see Fig. 25 in Howe, 2009, and accompanying discussion).

Numerous models have been proposed to explain the observed behavior of solar torsional oscillations, the vast majority relying directly or indirectly on the Lorentz force associated with the Sun’s magnetic field. Howe (2009) in §9.5 gives a succinct overview of these various theoretical explanations, which turn out to be difficult to confirm or refute on the basis of extant observations. Torsional oscillations having higher amplitudes near the surface and at high latitudes are certainly to be expected; subjected to a torque of a given magnitude (and of whatever origin), a ring of fluid centered on the solar rotation axis will experience greater angular acceleration if located high up in the envelope since its moment of inertia will be reduced through the lower density; and at a given depth, that same moment will also be smaller at higher latitude because of

the shorter moment arm, yielding again greater angular acceleration. At any rate, both the good phase locking with the magnetic activity cycle as measured, e.g. through the sunspot number, and the close tracking of the equatorially migrating band of rotational acceleration with the activity belts, point toward a close dynamical link between torsional oscillations and the cycling large-scale solar magnetic field. This has in fact remained the favored explanation ever since the discovery of torsional oscillations (Schuessler, 1981; Yoshimura, 1981). Interest in this possible dynamical linkage has in fact recently ramped up, due primarily to the curious observation that the poleward branch of the torsional oscillations, expected to appear in the final years of cycle 23, has failed to show up as expected. Taken together with other peculiar features of the extended activity minimum having followed cycle 23, this has prompted speculations regarding the possibility that the Sun is about to enter a phase of strongly suppressed magnetic activity, perhaps akin to the Maunder Minimum (Hill *et al.*, 2011).

From a dynamical point of view, the simplest hypothesis would be to assume that torsional oscillations are directly driven by the Lorentz force associated with the cycling large-scale magnetic component that we associate with the magnetic activity cycle, acting on the zonal flows as a time-varying perturbation of the global hydrodynamical (HD) balance setting the form of solar internal differential rotation. Such a balance would involve Reynolds stresses, Maxwell stresses, angular momentum advection by the meridional flow within the convection zone¹. As will become apparent in what follows, the situation may well be far more complex.

In this paper we present an analysis of the dynamics and energetics of torsional oscillations arising in a global magnetohydrodynamical (MHD) simulation of solar convection producing solar-like cycles in its dynamo-generated large-scale magnetic field. We first (§2) give an overview of the simulation itself together with a description of torsional oscillations arising therein. We then recast the azimuthal component of the momentum equation in conservative form, which allows the study of azimuthal force balance in terms of fluxes of angular momentum and their temporal variations (§3). We also examine the energetics of torsional oscillations, and conclude (§4) by elaborating on some consequences of our analysis for dynamo saturation, and for the possible use of torsional oscillations as precursors of cycle amplitude fluctuations.

2. Numerical data

2.1. The global simulation

We use numerical data produced by one of the global implicit large-eddy simulations of MHD solar convection of the type presented in Ghizaru, Charbonneau, and Smolarkiewicz (2010), and Racine *et al.* (2011). These remain so

¹Some level of dynamical coupling to the underlying stably stratified radiative core may also play important role; on the possible participation of the outer radiative core in setting the angular momentum balance within the convection zone, see the prescient analysis presented in Gilman, Morrow, and Deluca (1989).

far unique in producing an axisymmetric large-scale magnetic field component undergoing cyclic polarity reversals on a multi-decadal timescale, in a manner similar in many ways to what is observed on the sun. The underlying mathematical and computational frameworks are described in detail in Charbonneau and Smolarkiewicz (2012), and represent a MHD generalization of the well-proven general-purpose geophysical flow simulation code EULAG (see Prusa, Smolarkiewicz, and Wyszogrodzki, 2007, and references therein). An unique feature of both EULAG and EULAG-MHD is the possibility to delegate all dissipation to the underlying non-oscillatory forward-in-time advection scheme, which makes it possible to reach a maximally turbulent state at a given grid size, with stability persisting even when field gradients reach spatial scales commensurate with the computational cell size. As a consequence, turbulent simulations can be produced on relatively coarse grids, which allows very long time integration, as required in the study of behaviors such as magnetic cycles, which develop on timescales very much longer than the turbulent turnover time. The specific simulation segment analyzed in what follows spans 180 yr, and is executed on a relatively small mesh of size $N_r \times N_\theta \times N_\phi = 47 \times 64 \times 128$ in radius \times latitude \times longitude. The spatial domain is a thick spherical shell $0.62 \leq r/R \leq 0.96$ rotating initially rigidly at the solar rate, convectively unstable in its outer two thirds ($0.718 \leq r/R \leq 0.96$). The overall modelling framework is described in detail in Charbonneau and Smolarkiewicz, 2012, to which we refer the interested reader for further details.

The foregoing analysis begins with the four-dimensional data cubes (3 spatial dimensions plus time) returned by the simulation. The first step is to extract the axisymmetric components of the total flow and magnetic field. As shown in Racine *et al.* (2011) through modal decomposition, these axisymmetric components evolve on a timescale much longer than their non-axisymmetric counterparts, and can thus be legitimately considered as a distinct dynamical entity. We therefore express the total flow (\mathbf{U}) and magnetic field (\mathbf{B}) as

$$\mathbf{U}(r, \theta, \phi, t) = \mathbf{u}(r, \theta, t) + \mathbf{u}'(r, \theta, \phi, t) , \quad (1)$$

$$\mathbf{B}(r, \theta, \phi, t) = \mathbf{b}(r, \theta, t) + \mathbf{b}'(r, \theta, \phi, t) , \quad (2)$$

where

$$\mathbf{u}(r, \theta, t) = \langle \mathbf{U}(r, \theta, \phi, t) \rangle , \quad (3)$$

$$\mathbf{b}(r, \theta, t) = \langle \mathbf{B}(r, \theta, \phi, t) \rangle , \quad (4)$$

are the axisymmetric large-scale components, calculated by zonal averaging :

$$\langle \mathbf{X}(r, \theta, \phi, t) \rangle = \frac{1}{2\pi} \int_0^{2\pi} \mathbf{X}(r, \theta, \phi, t) d\phi . \quad (5)$$

Note that under these definitions, $\langle \mathbf{u}' \rangle = \langle \mathbf{b}' \rangle = 0$, so that the non-axisymmetric contributions of the flow and field play the role of the “small scales” in mean-field theory.

Figure 1 offers four views of the large-scale (axisymmetric) toroidal magnetic field components evolving over the timespan of the simulation. The top two

panels (A) and (B) show time-latitude cuts, the first extracted at the depth coinciding with the base of the convecting layers ($r/R = 0.718$), and the other near its top ($r/R = 0.94$). The bottom two panels show time-radius cuts extracted at (C) low and (D) mid-latitudes in the southern hemisphere. Regular polarity reversals of the large-scale magnetic field stand out prominently in these diagrams, here on a period of about 36 yr for each half cycle (equivalent to a sunspot cycle); thus the magnetic cycle period in this simulation is a little over three times longer than the $\simeq 11$ yr observed on the sun. The large-scale toroidal component is antisymmetric about the equatorial plane, in agreement with Hale's polarity laws, and peaks at mid-latitudes (panel A) and immediately beneath the core-envelope interface (panel D); this latter property is in line with the need to form and store in the convectively stable layer the toroidal magnetic flux ropes that, upon buoyancy-driven destabilization and emergence, will give rise to sunspots (see Fan, 2009, and references therein). The subsurface time-latitude diagram on panel (C) and time-radius diagram on panel (D) also show a hint of a secondary dynamo mode, of much shorter period and lower amplitude than the primary mode, producing what looks like an oscillation superimposed on the more slowly evolving magnetic component pervading the bulk of the domain. Interestingly, a similar combination of long- and short-period dynamo modes was also observed in the spherical wedge simulations of Käpylä *et al.* (2010). This intriguing dynamo feature will be revisited in what follows.

Other features of this simulation are discrepant with respect to the solar cycle, besides the period. Most notably, the toroidal magnetic component at the core-envelope interface, where sunspots are presumed to originate, peaks at too high latitudes compared to the sunspot butterfly diagram, and only shows a hint of equatorward migration. Moreover, analysis of the poloidal large-scale component reveals that the latter oscillates in phase with the deep-seated toroidal component, whereas in the sun a phase lag of $\pi/2$ is inferred. The specific simulation we are using for the foregoing analysis develops a slow phase drift between hemisphere, which eventually leads, after some 300 years, to a switch to a non-axisymmetric large-scale dynamo mode, a fascinating dynamo behavior in and of itself. Despite these departures with respect to observed solar behavior, the presence of a well-defined cyclic behavior in the large-scale magnetic field offers a unique opportunity to investigate quantitatively the magnetic backreaction on large-scale flows building up in the simulation and observed in the sun, in particular differential rotation.

2.2. The mean differential rotation

Mechanically-speaking, solar differential rotation is driven primarily by Reynolds stresses arising through rotation-driven anisotropies in convective turbulence, and angular momentum transport by meridional flows. Helioseismology has now mapped with good accuracy differential rotation throughout the bulk of the solar convection zone and upper radiative core (see, e.g., Fig. 18 in Howe, 2009). If one excludes subphotospheric layers, the primary rotational gradient in the solar convection zone is latitudinal, with the rotational frequency of equatorial region exceeding that of polar regions by about 30%. This latitudinal gradient vanishes

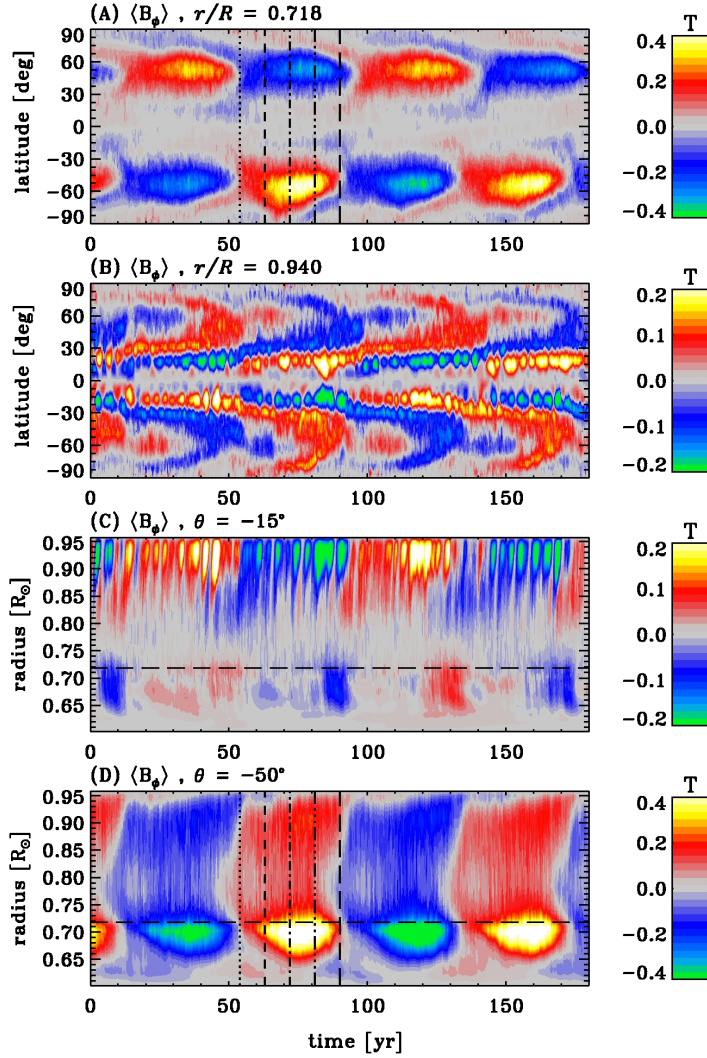


Figure 1. Two latitude-time representations of the zonally-averaged toroidal magnetic field at two different radii, along with two radius-time representations at two different latitudes. The dashed line in panels (C) and (D) represents the interface between the convectively stable and unstable fluid layers in the simulation's background stratification. The vertical lines in panels (A) and (D) flags five specific epochs across the second half-cycle, for subsequent reference.

at the interface between the convection zone and the underlying radiative core, across a thin shear layer known as the tachocline.

In the simulations, differential rotation can be directly computed from the zonally-averaged ϕ -component of the flow velocity. We first compute the mean differential rotation profile by temporally averaging over the full temporal extent of the simulation. We have carried out this averaging exercise for the MHD simulation of Fig. 1, as well as a purely HD convection simulation operating under the same forcing regime and rotation rate, and computed using the same mesh size. The results are shown on Figure 2, expressed as angular velocity $\Omega = \langle u_\phi \rangle / (r \cos \theta)$ with $-\pi/2 \leq \theta \leq \pi/2$ the latitude. The left panels show isocontour maps, with corresponding radial cuts plotted on the right panels, on the same scales to allow quick visual comparison of the two simulations. Both simulations are characterized by equatorial acceleration, but with isocontours too closely aligned with the rotation axis, and too concentrated towards the middle of the convection zone at low latitudes, as compared to the helioseismically-inferred solar internal differential rotation. These features are in fact typical of these types of simulations (see, e.g., Fig. 9 in Brun, Miesch, and Toomre, 2004; Fig. 1 in Browning *et al.*, 2006; Fig. 3 in Brown *et al.*, 2008), unless a latitudinal gradient in the heat flux is artificially imposed at the base of the domain (see Miesch, Brun, and Toomre, 2006). Nonetheless, the differential rotation characterizing the HD simulation (top row) shows some remarkably solar-like features, notably the magnitude of the pole-to-equator angular velocity contrast, and, in particular, a thin tachocline-like rotational shear layer located immediately beneath the core-envelope interface. The thinness of this layer ($\simeq 0.05R$ here) is a direct reflection of the very low dissipation levels characterizing this simulation (cf. Fig. 1 in Browning *et al.*, 2006).

The resemblance to solar differential rotation degrades, however, upon moving to the MHD simulation (bottom row on Fig. 2). The pole-to-equator angular velocity contrast is now reduced by a factor of three as compared to the HD simulation, and the latitudinal gradient has all but vanished at mid to high latitude. A residual tachocline remains, in the sense that the weak convection zone latitudinal differential rotation again vanishes across a thin shear layer beneath the core-envelope interface. Although quite weak, this remaining differential rotation remains important for the operation of the dynamo, as the analysis of a similar simulation carried out in Racine *et al.* (2011) shows that it contributes approximately equally with the turbulent electromotive force to the regeneration of the large-scale toroidal magnetic field near the core-envelope interface.

Another important difference between the differential rotation profiles characterizing the HD and MHD simulations is that the former is temporally steady once the simulation has attained a statistically stationary state, while the latter exhibit spatiotemporally coherent cyclic variations superimposing themselves on the mean rotational profile. We now turn to the characterization of these torsional oscillations.

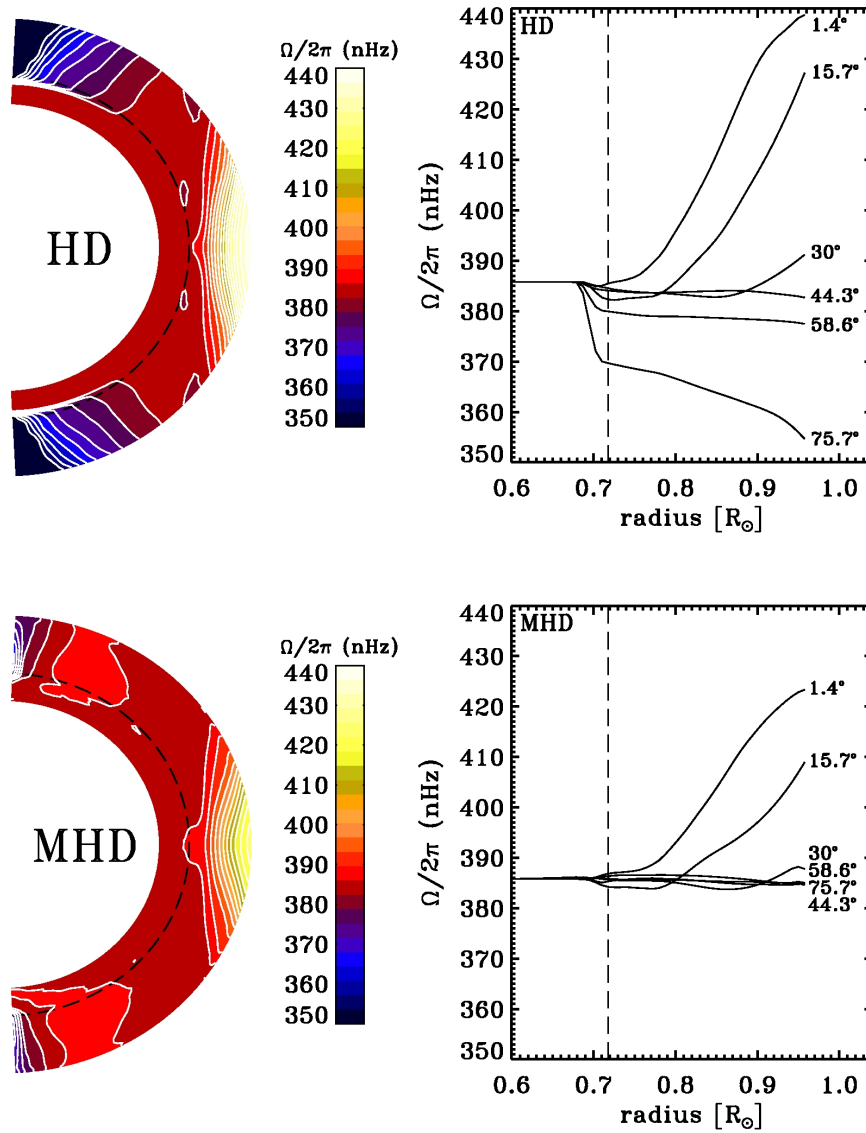


Figure 2. Two different representations of the angular velocity in a purely hydrodynamical simulation (top) and the MHD simulation of Fig. 1 (bottom). The left panels show contour plots of rotational frequency at each position in the Sun, constructed from the zonally-averaged longitudinal velocity averaged in time over the duration of the simulation. The right panels show the same results in the form of constant-latitude radial cuts, highlighting the presence of a tachocline-like shear layer immediately beneath the core-envelope interface ($r/R = 0.718$, dashed line).

2.3. The torsional oscillations

Torsional oscillations are best visualized by subtracting the temporally-averaged rotational frequency profile of Fig. 2 from the corresponding zonally-averaged rotational frequency at each time step :

$$\langle \Delta\omega \rangle(r, \theta, t) = (2\pi r \cos \theta)^{-1} (u_\phi(r, \theta, t) - \bar{u}_\phi(r, \theta)) , \quad (6)$$

where the overbar denotes temporal averaging over the time span of the simulation :

$$\bar{u}_\phi(r, \theta) = \frac{1}{2\pi T} \int_0^T \int_0^{2\pi} U_\phi(r, \theta, \phi, t) d\phi dt , \quad (7)$$

amounting to the zonal and temporal average of the full azimuthal velocity $U_\phi(r, \theta, \phi, t)$ data cube, with T the length of the simulation. The result of this procedure is shown on Figures 3 and 4, which display respectively time-latitude diagrams at four fixed depths, and radius-latitude diagrams at four fixed latitudes. Several features visible in these plots are noteworthy: (1) A cyclic signal is clearly present at all depths and latitudes so sampled, at twice the frequency characterizing the magnetic cycle (cf. Fig. 1); (2) The torsional oscillations peak in amplitude at high latitudes and in the surface and subsurface layers, reaching there $\simeq 3$ nHz; (3) At mid- to high latitudes, the oscillations show a phase approximately independent of depth. The oscillations reach their peak prograde phase (i.e., $\langle \Delta\omega \rangle$ peaking at positive values) at about the peak of the magnetic cycle. All these features are remarkably solar-like, as can be inferred from comparison with similarly-formatted diagram in Howe (2009; cf. her Fig. 26 to Fig. 4 herein).

At first glance, the surface spatiotemporal pattern of the torsional oscillations is not particularly solar-like (cf. Fig. 25 of Howe, 2009, and Fig. 3D herein). Near the surface, a strong and rather complex oscillatory signal is present at low latitudes, arising from the superposition of an oscillation associated with the large-scale magnetic cycle with a second, characterized by higher frequency oscillations and restricted to the subsurface equatorial regions. Examinations of the simulation reveals that this is associated with a secondary dynamo mode feeding on the strong latitudinal shear present in the outer half of the convection zone at low latitudes (see Fig. 2; also Fig. 1B,C).

However, the dissimilarities greatly diminish if one focuses on the pattern present at latitudes higher than the magnetic “activity belts”. Figure 5 illustrates the idea. It is essentially a closeup of the northern hemisphere portion of Fig. 3C, on which have been superimposed a few isocontours of mean toroidal magnetic field strengths at the core-envelope interface (cf. Fig. 1A) for the first three half-cycles in the simulation. This stretching procedure “renormalizes” the activity belts to low latitudes, and allows a comparison that is arguably more relevant to the patterns observed on the sun. If one accepts this stretch at face value, then the comparison becomes actually quite good (cf., e.g., Fig. 25 in Howe, 2009). In particular, the torsional acceleration ($\langle \Delta\omega \rangle > 0$) is seen to begin at high latitude (here $\simeq 70^\circ$) at about the time of magnetic polarity reversal (akin

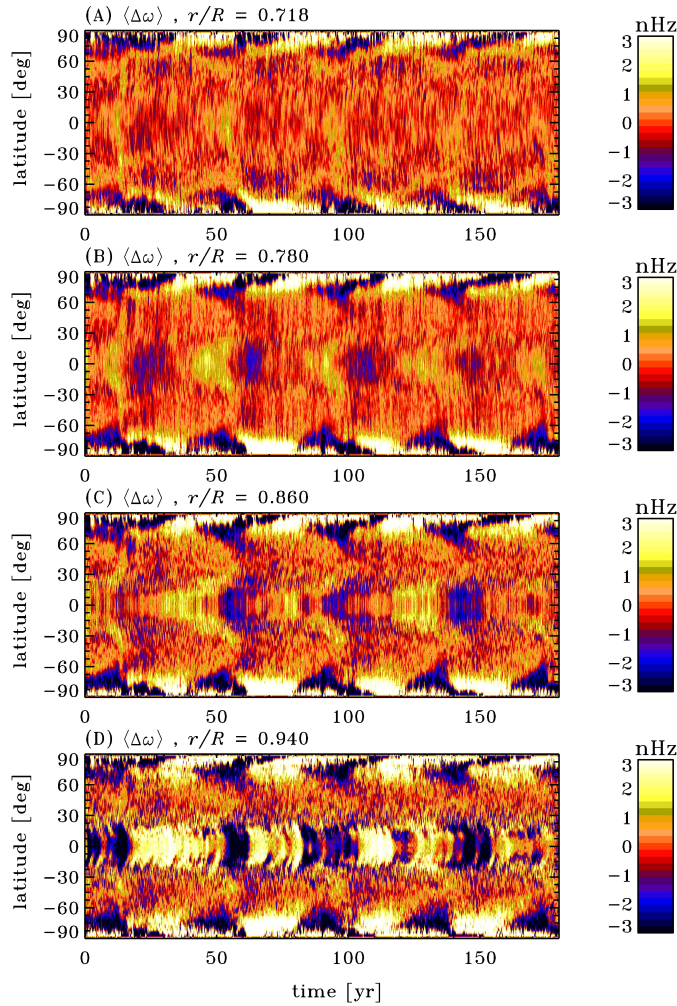


Figure 3. Time-latitude diagrams of the zonally-averaged perturbation in rotational frequency, at four different depths in the simulation. Positive (negative) perturbations correspond to rotational acceleration (deceleration) with respect to the mean state plotted on Fig. 2B

to solar minimum here), and develops in two diverging branches, one propagating poleward and the second, of lower amplitude, propagating equatorward. In the sun, this second branch requires two activity cycles to reach the equator, while here it does so in only one cycle; this may be a reflection of the fact that our activity belts are located at too high latitudes, but this remains to be demonstrated through further simulations. It is also quite remarkable that this

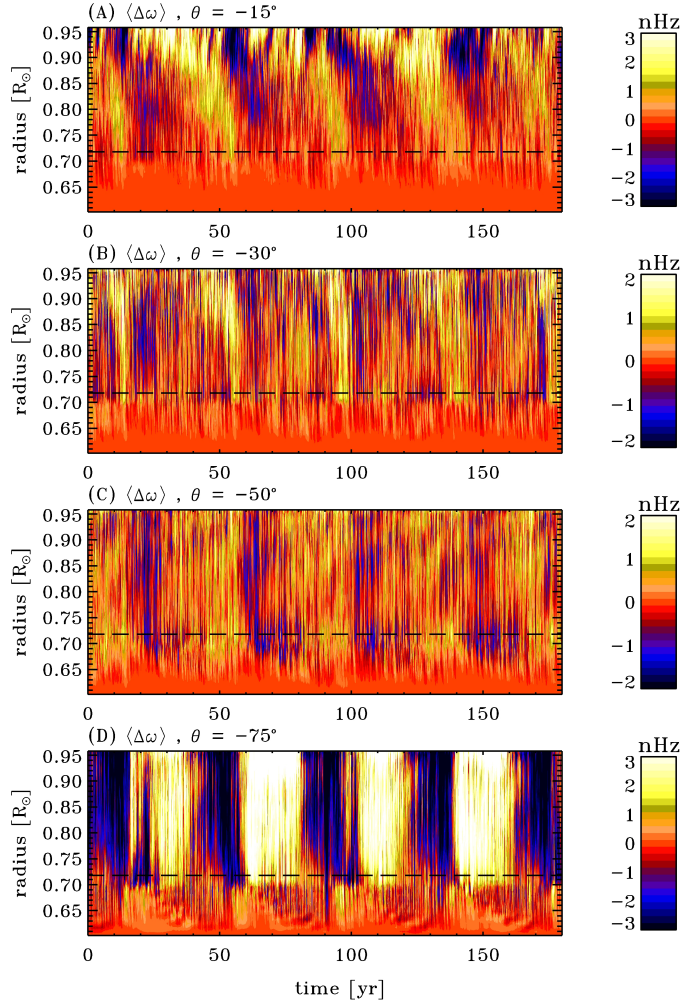


Figure 4. Time-radius diagrams of the zonally-averaged perturbation in rotational frequency, at four different latitudes in the simulation. The dashed line indicates the position of the core-envelope interface.

latitudinal double-branch pattern in the torsional oscillations persists all the way to the base of the convecting layers in the simulation. Careful examination of Fig. 4D also reveals that an oscillatory signal even penetrates all the way through the underlying stably-stratified layer to the base of the computational domain ($r/R = 0.62$), although this signal may reflect the excitation of gravity waves.

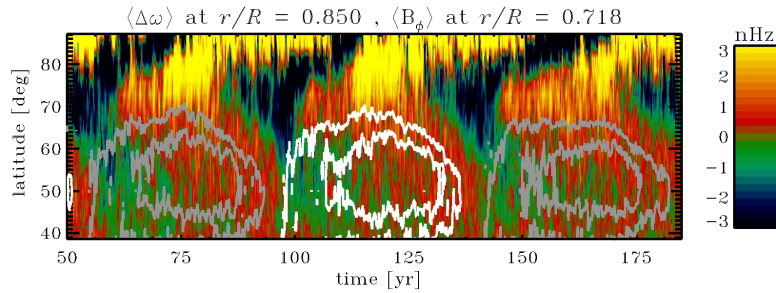


Figure 5. A close up on the time-latitude diagram of Fig. 3D, showing the zonally-averaged rotational frequency perturbation. The color scale and range are now chosen identical to those used in Fig. 25 of Howe (2009), to ease comparison. A few isocontours of zonally-averaged toroidal field at the core-envelope interface ($r/R = 0.718$) have been superimposed, to indicate the relative phase of the magnetic cycle. White (grey) correspond to positive (negative) toroidal field, and the innermost contours has value ± 0.2 T.

At any rate, the results presented here demonstrate clearly that this simulation generates a global torsional oscillation pattern that is solar-like in a number of ways. Remaining discrepancies notwithstanding, we have in hand a unique “virtual laboratory” allowing a quantitative and fully dynamical investigation of the mechanism(s) driving these torsional oscillations. This is the topic to which we now turn.

3. The dynamical drivers of torsional oscillations

3.1. The zonal momentum equation

Torsional oscillations are generated because the (magneto)dynamics of the convecting layers lead to a systematic, time-dependent redistribution of angular momentum that is driven, directly or indirectly, by the magnetic cycle. In parallel to the MHD equations solved in the simulation, the foregoing analysis focuses on the azimuthal component of the Navier-Stokes equations, including the Lorentz and Coriolis forces, and written under the anelastic approximation. The latter implies, in particular, that mass conservation reduces to $\nabla \cdot (\rho \mathbf{U}) = 0$.

The starting point of our analysis is to recast the azimuthal momentum equation in conservative form involving fluxes of angular momentum. We begin by applying the azimuthal averaging operator previously defined in eq. (5)

$$\left\langle \frac{\partial(\rho U_\phi)}{\partial t} \right\rangle + \langle [\nabla \cdot (\rho \mathbf{U} \mathbf{U})]_\phi \rangle = -\frac{1}{r \cos \theta} \left\langle \frac{\partial P}{\partial \phi} \right\rangle + \frac{1}{\mu_0} \langle [(\nabla \times \mathbf{B}) \times \mathbf{B}]_\phi \rangle, \quad (8)$$

with $\mathbf{U} = \mathbf{V} + \boldsymbol{\Omega} \times \mathbf{R}$, where \mathbf{V} is the velocity field of the plasma in the rotating frame of the Sun, $\boldsymbol{\Omega}$ is the mean angular velocity of the Sun, \mathbf{R} is a radial vector locating a given fluid element in a spherical coordinate system with origin at the Sun’s center, and once again the variable θ denotes the latitude. Now, the azimuthal averaging operator commutes with derivatives

acting on large-scale quantities, and the Lorentz force term can be rewritten as $(\nabla \times \mathbf{B}) \times \mathbf{B} = (\mathbf{B} \cdot \nabla) \mathbf{B} - \frac{1}{2} \nabla B^2$. Moreover, under the axisymmetry assumption, all azimuthal derivatives of averaged quantities automatically vanish, so that the above expression reduces to:

$$\frac{\partial \langle \rho U_\phi \rangle}{\partial t} + \langle \hat{\phi} \cdot [\nabla \cdot (\rho \mathbf{U} \mathbf{U})] \rangle = \frac{1}{\mu_0} \langle \hat{\phi} \cdot (\mathbf{B} \cdot \nabla) \mathbf{B} \rangle . \quad (9)$$

Use of judicious vector identities also lead to:

$$\langle \hat{\phi} \cdot [\nabla \cdot (\rho \mathbf{U} \mathbf{U})] \rangle = \frac{1}{r \cos \theta} \nabla \cdot (r \cos \theta \bar{\rho} \langle U_\phi \mathbf{U} \rangle) , \quad (10)$$

$$\langle \hat{\phi} \cdot [(\mathbf{B} \cdot \nabla) \mathbf{B}] \rangle = \frac{1}{r \cos \theta} \nabla \cdot (r \cos \theta \langle B_\phi \mathbf{B} \rangle) , \quad (11)$$

where $\bar{\rho}(r)$ is simply the density in the reference state, that substitution being consistent with the anelastic approximation.

Using the scale separation introduced in eq. (1)–(2), the various terms can be separated between large-scale and small-scale contributions, e.g.:

$$\langle U_\phi \mathbf{U} \rangle = \langle (u_\phi + u'_\phi)(\mathbf{u} + \mathbf{u}') \rangle = u_\phi \mathbf{u} + \langle u'_\phi \mathbf{u}' \rangle , \quad (12)$$

and likewise for $\langle B_\phi \mathbf{B} \rangle$. Rewriting eq. (10), eq. (11) and assembling them in eq. (9) while using the previous identities gives

$$\frac{\partial(\bar{\rho} u_\phi)}{\partial t} - \frac{1}{r \cos \theta} \nabla \cdot \left[r \cos \theta \left(\frac{1}{\mu_0} (b_\phi \mathbf{b} + \langle b'_\phi \mathbf{b}' \rangle) - \bar{\rho} (u_\phi \mathbf{u} + \langle u'_\phi \mathbf{u}' \rangle) \right) \right] = 0 . \quad (13)$$

Changing now to the co-rotating reference frame implies $\mathbf{u} = \mathbf{v} + \boldsymbol{\Omega} \times \mathbf{r}$ and $\mathbf{u}' = \mathbf{v}'$ because there is no small-scale contribution to $\boldsymbol{\Omega} \times \mathbf{r}$. Since the latter term is also divergenceless, we can write:

$$u_\phi \mathbf{u} = (v_\phi + \Omega r \cos \theta) \mathbf{v} . \quad (14)$$

The end result of all this is to recast eq. (13) in conservative form :

$$\begin{aligned} \frac{\partial(\bar{\rho} v_\phi)}{\partial t} - \frac{1}{r \cos \theta} \nabla \cdot \left[r \cos \theta \left(\frac{1}{\mu_0} (b_\phi \mathbf{b} + \langle b'_\phi \mathbf{b}' \rangle) - \right. \right. \\ \left. \left. - \bar{\rho} ((v_\phi + \Omega r \cos \theta) \mathbf{v} + \langle v'_\phi \mathbf{v}' \rangle) \right) \right] = 0 . \end{aligned} \quad (15)$$

Notice that $\partial_t(\bar{\rho} v_\phi)$ is in fact a volumic force density in the longitudinal direction, as expressed in the rotating frame. The four terms adding up under the divergence are the four contributors to zonal dynamics :

$$F_{\text{Reyn}} = \frac{-1}{r \cos \theta} \nabla \cdot (r \cos \theta \bar{\rho} \langle v'_\phi \mathbf{v}' \rangle) , \quad (16)$$

$$F_{\text{Circ}} = \frac{-1}{r \cos \theta} \nabla \cdot (r \cos \theta \bar{\rho} (v_\phi + \Omega r \cos \theta) \mathbf{v}) , \quad (17)$$

$$F_{\text{Maxw}} = \frac{1}{r \cos \theta} \nabla \cdot \left(\frac{r \cos \theta}{\mu_0} \langle b'_\phi \mathbf{b}' \rangle \right) , \quad (18)$$

$$F_{\text{Magn}} = \frac{1}{r \cos \theta} \nabla \cdot \left(\frac{r \cos \theta}{\mu_0} b_\phi \mathbf{b} \right), \quad (19)$$

These are, respectively, turbulent Reynolds stresses, Coriolis force acting on the meridional flow, turbulent Maxwell stresses (small-scale Lorentz force) and the magnetic torque (Lorentz-force associated with large-scale magnetic component). Note that viscous stresses do not appear explicitly here, as our simulation is of the implicit large-eddy type, i.e., it does not include explicit dissipative terms in the momentum equation.

3.2. Angular momentum fluxes

As per eq. (15), the mean radial and latitudinal angular momentum fluxes are given by:

$$\begin{aligned} \mathcal{L}_r(r, \theta, t) = & r \cos \theta \left(\frac{1}{\mu_0} (b_\phi b_r + \langle b'_\phi b'_r \rangle) - \right. \\ & \left. - \bar{\rho}((v_\phi + \Omega r \cos \theta)v_r + \langle v'_\phi v'_r \rangle) \right), \end{aligned} \quad (20)$$

$$\begin{aligned} \mathcal{L}_\theta(r, \theta, t) = & r \cos \theta \left(\frac{1}{\mu_0} (b_\phi b_\theta + \langle b'_\phi b'_\theta \rangle) - \right. \\ & \left. - \bar{\rho}((v_\phi + \Omega r \cos \theta)v_\theta + \langle v'_\phi v'_\theta \rangle) \right). \end{aligned} \quad (21)$$

Following Brun, Miesch, and Toomre (2004), we first examine the global rotational dynamics by computing from the simulation output the fluxes of angular momentum integrated across spherical shells or conical wedges centered on the rotation axis:

$$I_r(r, t) = \int_{-\pi/2}^{\pi/2} \mathcal{L}_r(r, \theta, t) r^2 \cos \theta \, d\theta, \quad (22)$$

$$I_\theta(\theta, t) = \int_{r_{\text{bot}}}^{r_{\text{top}}} \mathcal{L}_\theta(r, \theta, t) r \cos \theta \, dr, \quad (23)$$

so that $I_r(r, t)$ is the net angular momentum transport rate through shells of different radii, and $I_\theta(r, t)$ through cones tangent to different latitudes.

In order to disentangle the various physical contribution to angular momentum transport, these integrals are computed separately for the four distinct contributions to the total angular momentum fluxes. The result of this procedure is shown in Figure 6, where the fluxes have also been temporally averaged over the extent of the simulation. The procedure was also carried out for the same parent hydrodynamical simulation whose mean rotational frequency is plotted on Fig. 2 (top). In this HD simulation, the only contributors to zonal dynamics are the Reynolds stresses and Coriolis force acting on the meridional flow.

In the HD simulation, the Reynolds stresses and Coriolis force are seen to act in opposition at all latitudes and depths. This is precisely what one would expect for a stationary rotational state to ensue. With all fluxes vanishing at domain boundaries, the fact that these two contributions do not add up to zero

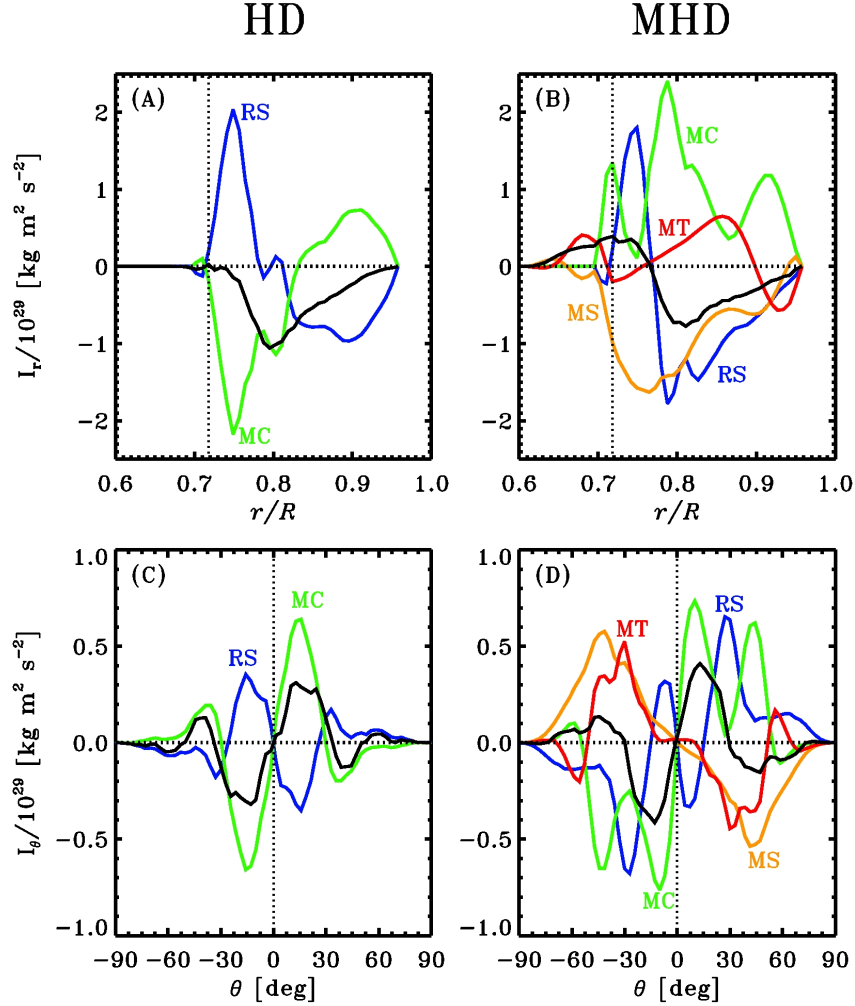


Figure 6. A four panels diagram showing angular momentum flux contributions. Panels (A) and (C) show these contributions in the HD simulation, while panels (B) and (D) show them in the MHD simulation. Panels (A) and (B) represent angular momentum fluxes through spherical shells of different radii, with positive fluxes amounting to upwards transport of angular momentum. Panels (C) and (D) show the fluxes through conical surfaces of different latitudes, with positive values indicating northward transport. The various curves are color-coded as follows : blue - Reynolds stresses; green - Coriolis force; orange - Maxwell stresses; red - large-scale magnetic fields; black - total of all the contributions. The vertical dotted lines in the top two panels show the location of the core-envelope interface at $r/R = 0.718$.

reflects the presence, in the simulation, of a dissipative force associated with the numerical scheme, which here contributes significantly to the zonal dynamics, especially at low latitudes in the convection zone. This can be traced in part to the very strong rotational shear which builds up there in the HD simulation (cf. top panels Fig. 2).

Turning to the MHD simulation, the most obvious feature is perhaps the fact that all four potential fluxes of angular momentum contribute more or less equally to the global rotational dynamics. Moreover, the presence of magnetic fields has greatly altered the non-magnetic fluxes of angular momentum. This is particularly the case for the radial flux of angular momentum associated with the Coriolis force (cf. green curves on panels A and B), and latitudinal fluxes by Reynolds stresses (cf. blue curves on panels C and D), which both undergo reversals in direction over a substantial portion of their spatial range when going from HD to MHD. Also noteworthy in this MHD simulation, the Maxwell stresses associated with the small-scale magnetic field contribute more or less equally to the Lorentz force associated with the large-scale, cycling magnetic field. Finally, the presence of a magnetic field leads to a significant rotational coupling between the convection zone and underlying stably stratified core, extending deep into the latter. Such a coupling is almost entirely absent in the HD simulation. Note finally that the high degree of (anti)symmetry about the equator apparent on panels (C) and (D) is a true feature of these simulations, as no averaging of hemispheres has been carried out here.

It is particularly interesting to compare Figs. 6B and D to the corresponding diagrams presented in Brun, Miesch, and Toomre (2004), namely their Fig. 10². Their simulation differs from ours in three important ways: (1) it covers only the convecting layers; (2) it includes substantial explicit viscosities and magnetic diffusivities throughout the simulation domain; and (3) it does not generate a large-scale magnetic component. Even though their mean differential rotation is qualitatively similar to ours (equatorial acceleration, polar deceleration, tendency towards cylindrical isocontours in equatorial regions), major differences exist in the underlying rotational dynamics. Viscous forces play a major role in the radial transport of angular momentum in their simulation, teaming with Maxwell stresses to offset the Coriolis force and Reynolds stresses throughout the whole convection zone. In our simulation, this dynamical balance (minus viscous force) materializes only in the lower third of the convecting layers, with Reynolds and Maxwell stresses acting in opposition to the Coriolis force higher up. In both simulations, the latter leads to a net upward transport of angular momentum, and Maxwell stresses drive a downward transport.

For the simulation analyzed on Fig. 10 of Brun, Miesch, and Toomre (2004), viscous diffusion makes a lesser contribution to angular momentum transport in the latitudinal direction than it does in the radial direction, and not surprisingly there are now more similarities with our latitudinal fluxes, Reynolds and Maxwell stresses now opposing each other at most latitudes. The primary difference, beside the presence of a significant large-scale magnetic torque in our simulation,

²Note that in Brun, Miesch, and Toomre (2004) their equivalent of our integrated radial fluxes are divided by R^2 and they are using CGS units instead of SI units.

is found with the net latitudinal angular momentum transport by the meridional flows, which is poleward at most latitudes in our simulation, but equatorward in Brun, Miesch, and Toomre (2004) simulations.

The differences between these two sets of simulations most likely do not arise exclusively from the presence of a large-scale cyclic magnetic field in our simulations, as angular momentum fluxes calculated in purely HD versions of the Brun, Miesch, and Toomre (2004) simulations (see Miesch, 2000 and Brun and Toomre, 2002) also differ markedly from the HD balance depicted on Fig. 6A,C herein. Looking at case C in Fig. 11 from Brun and Toomre (2002), which is the most turbulent and closest to our parameter regime, and comparing it with our Figs. 6A,C, we observe very different patterns for both the Reynolds stresses and the Coriolis force acting on the meridional flow. The radial fluxes show distinct depth variations, particularly in the middle of the convection zone, but the difference is most striking in the latitudinal fluxes distributions, inverted. When looking at latitudes located in the range $-30^\circ \leq \theta \leq 30^\circ$ in Fig. 6C and Fig. 11C from Brun and Toomre (2002), both the Reynolds stresses and the meridional circulation contributions are of opposite sign when comparing both simulations together. Additionally, there is a sign change around $\pm 30^\circ$ in our simulation that has no counterpart in theirs. Brown *et al.* (2008) present another set of HD simulations, all strongly turbulent but where they also vary the rotation rate. More specifically, in their Fig. 9 they show angular momentum fluxes for two cases: $\Omega = \Omega_\odot$ in panels (A) and (B), and $\Omega = 5\Omega_\odot$ in (C) and (D). While panels (A) and (B) remain similar to the aforementioned equivalent plots in Brun and Toomre (2002), the more rapidly rotating case (panels C and D) reveal yet again a distinct dynamical balance. The major players in the radial transport of angular momentum are the Reynolds stresses and the viscous transport terms, with the Coriolis force exerted on the meridional circulation playing a lesser role. While latitudinal transport has a very complex profile, the Reynolds stresses and meridional circulation terms usually have the same sign and are counterbalanced by the viscous transport.

Another major difference lies of course with the fact that our dynamical balance is not perfectly stationary, showing instead periodic variations which drives the torsional oscillations visible on Figs. 3 and 4. It is therefore also interesting to examine the temporal evolution of those angular momentum fluxes over a magnetic half-cycle. This is carried out on Figure 7, which shows the evolution of each individual flux component, from the beginning of the second half-cycle on Fig. 1 to its end, i.e. from one minimum to the next, at a 9 yr temporal cadence, as indicated by the vertical line segments on Fig. 1A and D. Each panel also reproduces the temporal average of the corresponding contribution over the full simulation duration (in black), taken directly from Fig. 6B.

The magnetic torque contribution (panel D) shows large variations about its temporal average, which is of course expected in view of the cyclic evolution characterizing the large-scale magnetic field. Far less expected a priori, however, is the fact that all other flux contributions also undergo similar variations in the bulk of the convecting layers. This is even the case for the nominally non-magnetic contributions, namely the turbulent Reynolds stresses and Coriolis force acting on the meridional flow. The latter's temporal variations show little

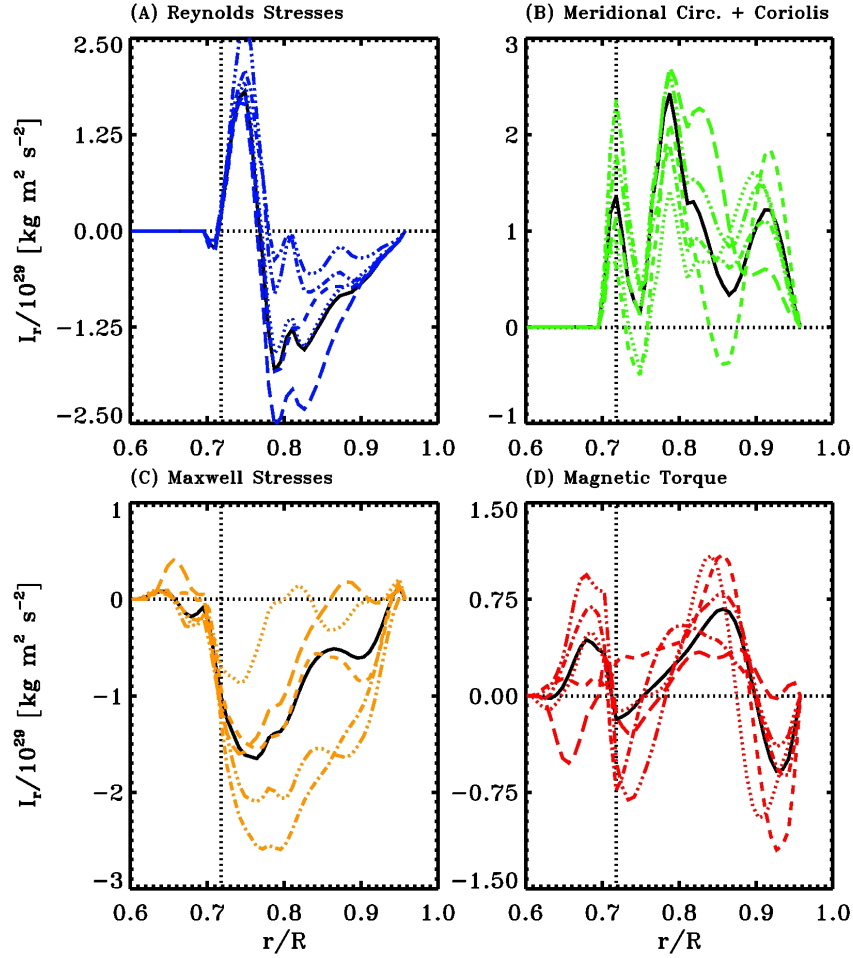


Figure 7. Temporal evolution of the various radial angular momentum flux contributions sampled at a 9 yr cadence between 54 and 90 yr: dotted $t = 54$ yr; short-dashed $t = 63$ yr; dot-dashed $t = 72$ yr; triple-dot-dashed $t = 81$ yr; long-dashed $t = 90$ yr, indicated by the correspondingly coded vertical line segments on Fig. 1A and D. The solid line is the corresponding flux contribution averaged over the entire simulation time. Note the varying vertical scales on the four panels.

spatial coherence, whereas Reynolds stresses vary largely in unison at all depths. A similar situation arises with the magnetic contributions, with the magnetic torque showing a complex spatiotemporal behavior, while temporal variations in Maxwell stresses are very well-correlated spatially. Also noteworthy, flux contributions associated with the small-scale flow and magnetic field —Reynolds and Maxwell stresses— fall rapidly with depth at and below the core-envelope interface, where they show almost no temporal variability. Consequently, the time-dependence of the rotational coupling between the convection zone and underlying stably stratified fluid layers is driven by the interplay between the strongly time-varying contributions of large-scale magnetic torques and angular momentum advection by the meridional flow.

The most important take-home message offered by Fig. 7 is the following : torsional oscillations are not driven by a cyclic, magnetically-mediated perturbation superimposing itself on an otherwise steady hydrodynamical balance. All angular momentum flux contributions, including those of a purely hydrodynamical nature, are strongly modulated by the magnetic cycle. In these simulations, torsional oscillations are a fully nonlinear and truly MHD phenomenon.

Another interesting aspect of our results relates to the rotational coupling between the convection zone, where differential rotation is generated, and the underlying stably-stratified nominally stable fluid layers. Figure 8A shows time series of the radial fluxes of angular momentum, computed via eq. (22) separately for each of its four contributions, as labeled. At the core-envelope interface proper ($r/R = 0.718$), the net transport of angular momentum across the corresponding spherical shell is directed upward, and is driven primarily by the Coriolis force acting on the meridional flow, and resisted by the magnetic forces. Although the magnitude of the the large-scale magnetic torque varies cyclically in phase with the magnetic cycle, as one would have expected, the Coriolis term does also, which results in a net upward flux of angular momentum (in black) that does not show a well-defined cyclic signal. This general pattern is maintained down to $r/R \simeq 0.70$ in the stable layers, but with the disappearance of the HD forces further below the magnetic terms take over completely, as shown on Figure 8B. The large-scale torque now drives an upward angular momentum flux, and is opposed by the Maxwell stresses. Cyclic variations on the magnetic cycle frequency can still be detected, but quasi-cyclic modulations on shorter periods are also apparent at these depths.

A similar dynamical transition as a function of depth in the stable layer is also present in the latitudinal angular momentum fluxes, as illustrated on Fig. 8C,D. These time series result from the calculation of the four individual contributions on the RHS of eq. (21) at latitude -45° and two different depths, as labeled. At the mid-latitude core-envelope interface ($r/R = 0.718$, panel C), the latitudinal flux is directed equatorward and dominated by the meridional flow contribution, which shows a strong cyclic signal in phase with the magnetic cycle. This is associated with a strong driving of the meridional flow by the large-scale magnetic field (on this point see also Passos, Charbonneau, and Beaudoin, 2012), but with regards to the zonal dynamics, the large-scale magnetic torque here drives angular momentum poleward, as expected from the shearing of a latitudinally-oriented poloidal large-scale magnetic field by a latitudinal differential rotation

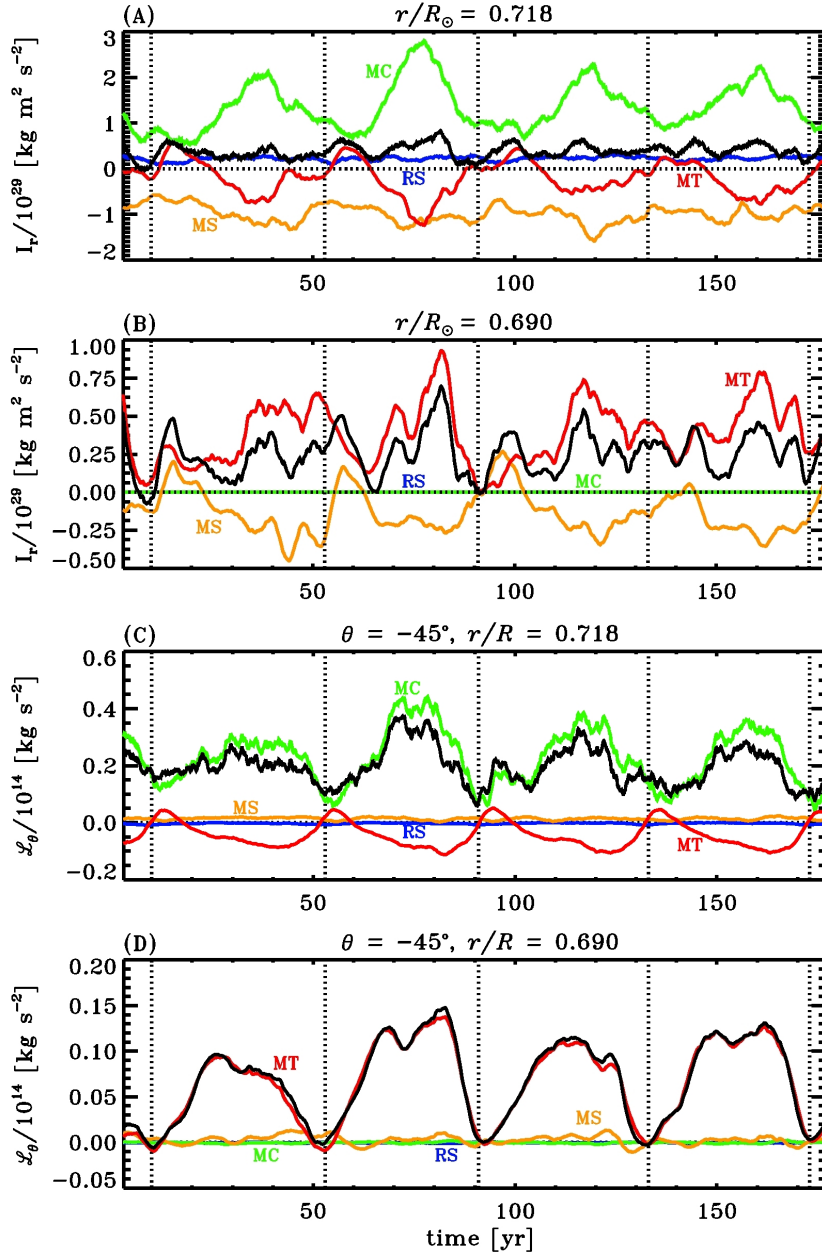


Figure 8. Temporal evolutions of angular momentum fluxes for each contribution. Panels (A) and (B) show the net radial angular momentum transport rate through spherical shells at $r/R = 0.718$ and $r/R = 0.69$. Panels (C) and (D) display time series of the mean latitudinal flux at these same depths, both at $\theta = -45^\circ$. Note the varying vertical scales on panels (A) vs (B), and (C) vs (D). The vertical dotted lines indicate epochs of polarity reversal of the large-scale internal toroidal magnetic field, as determined from Fig. 1, equivalent here to “solar minimum”. Here each time series has been smoothed with a boxcar average of width 4 yr.

characterized by equatorial acceleration. Moving inwards, already at $r/R = 0.70$ (not shown) the magnetic torque has reversed and now drives angular momentum equatorward, and by $r/R = 0.69$ (panel D) the contribution of the meridional flow has vanished and the large-scale magnetic torque is the sole driver of the equatorward angular momentum flux, which remains strongly modulated by the magnetic cycle. The Reynolds and Maxwell stresses are minor contributors to the latitudinal flux of angular momentum at all depths in the stable layer.

3.3. Volumic force densities

We now turn to explicit calculations of volumetric force densities, by taking the divergence of the various contributions to the total angular momentum flux, as appearing on the RHS of eq. (15), at each grid point in the meridional $[r, \theta]$ plane. In both HD and MHD simulations, temporally averaging each set of grid point values over four magnetic half-cycles produces again patterns with a high degree of symmetry with respect to the equator. Comparing HD and MHD simulations reveals the most pronounced differences at mid- to high latitudes, where even the nominally HD forces —Reynolds stresses and Coriolis force acting on the meridional flow— show large differences in their spatial distributions. This is particularly striking in the Coriolis term, which tends to accelerate (decelerate) the zonal flow in the outer (inner) half of the convecting layers of the HD simulation, and shows the opposite pattern in the MHD simulation. In the MHD simulation, Maxwell and Reynolds stresses tend to oppose each other at most locations in the meridional plane, and the two magnetic contributions are the sole significant contributors within the underlying stable fluid layer, consistent with Fig. 6.

Figure 9A offers a more focused look at the torsional oscillation dynamics at high latitudes, in the form of time series of the various azimuthal force components extracted at a specific grid point located at depth $r/R = 0.925$ and -70° latitude (Southern hemisphere). At first glance, at this location the Reynolds and Maxwell stresses contribute very little to the zonal dynamics, which is primarily driven by the large-scale Lorentz force (red) and Coriolis force (green). However, these two contributions are of similar magnitudes but strongly anticorrelated, and so nearly cancel each other. The resulting total force (black) is then of much smaller magnitude than either of these two contributions, and comparable again to the lower amplitude Maxwell stresses (orange).

Figure 9B replicates the temporal evolution of this net force, together with the evolution of the mean toroidal magnetic component (red) and zonal flow speed (blue). The red dashed line is a time series of the large-scale toroidal field extracted at mid-latitudes at the core-envelope interface, and represents here a proxy of the overall cycle phase. Despite strong temporal fluctuations, the plot reveals that the net zonal force is generally in the prograde direction throughout the peak phases of the magnetic cycle, and tends to fluctuate about zero around epochs of polarity reversals in the large-scale magnetic field. This is consistent with the peak prograde amplitude of torsional oscillations occurring around times of cycle maximum (cf. Figs. 1 and 4). The fact that the local variation of the toroidal field lags behind the zonal flow variations suggests that

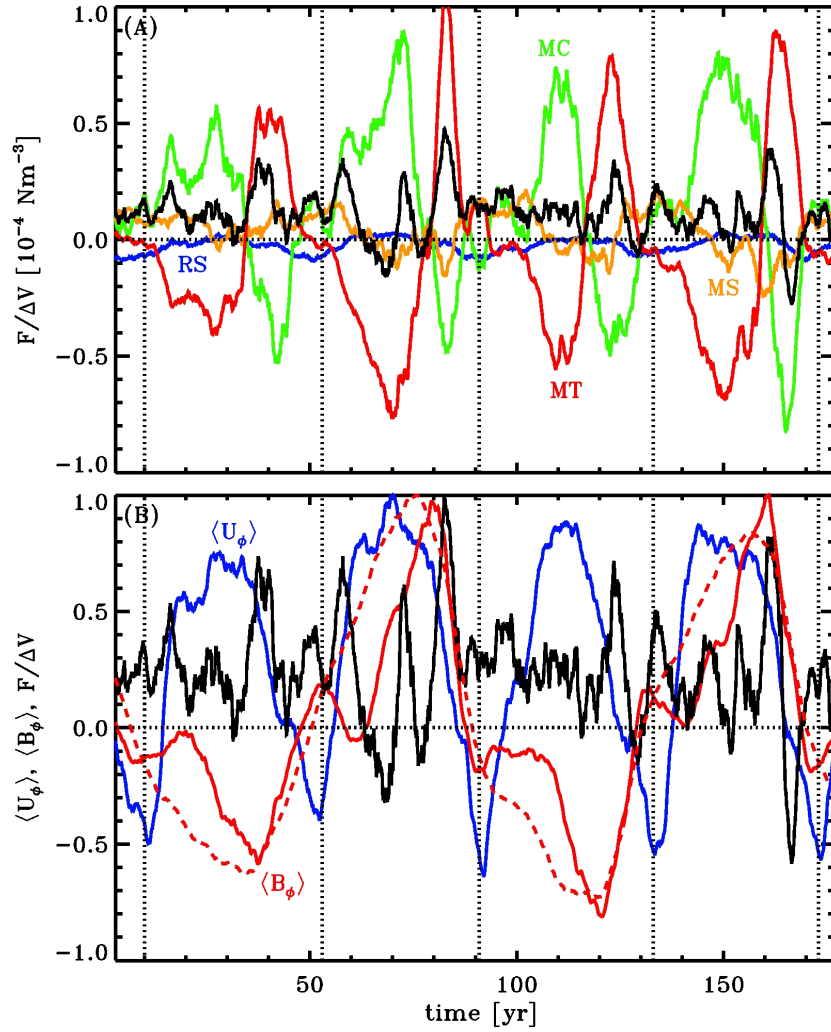


Figure 9. Two representations of temporal evolution of the total force applied on the plasma at $r/R = 0.925$ at a latitude of -70° . Panel (A) depicts individual force components : blue - Reynolds stresses; green - meridional circulation with Coriolis effect; orange - Maxwell stresses; red - large-scale magnetic fields; black - sum of all four contributions. The vertical dotted line indicate times of magnetic cycle minimum, based on the zonally-averaged toroidal field at the core-envelope interface (cf. Fig. 1). Panel (B) shows time series of the total force (black), the zonal velocity (blue) and toroidal magnetic field (red). The red solid line is the toroidal magnetic field taken at $r/R = 0.925$, $\theta = -70^\circ$, while the red dashed line is that same quantity extracted at $r/R = 0.718$, $\theta = -60^\circ$. Here each time series has been normalized to its peak values for comparison purposes, and smoothed with a boxcar average of width 4 yr. The vertical dotted lines delineate subsequent magnetic half-cycles.

the latter's shearing action contributes at least in part to its induction. It is quite remarkable that the force component in (A) which shows the best correlation with the zonal flow variations is the Reynolds stresses (blue), which have the lowest individual amplitude of all four force components.

Figure 10 offers yet a different look at the torsional oscillations dynamics. The curves are trajectories in a two-dimensional phase space defined in terms of the zonally-averaged zonal flow deviation about its temporal mean over the simulation span (horizontal), versus the zonally-averaged latitudinal flow deviation about its own temporal mean (vertical). Four such trajectories are shown, for meridional plane grid points located at the subsurface high latitudes $(r/R, \theta) = (0.95, \pm 70^\circ)$ in panels (A) and (B), and mid-high-latitude core-envelope interface $(r/R, \theta) = (0.718, \pm 60^\circ)$ in panels (C) and (D).

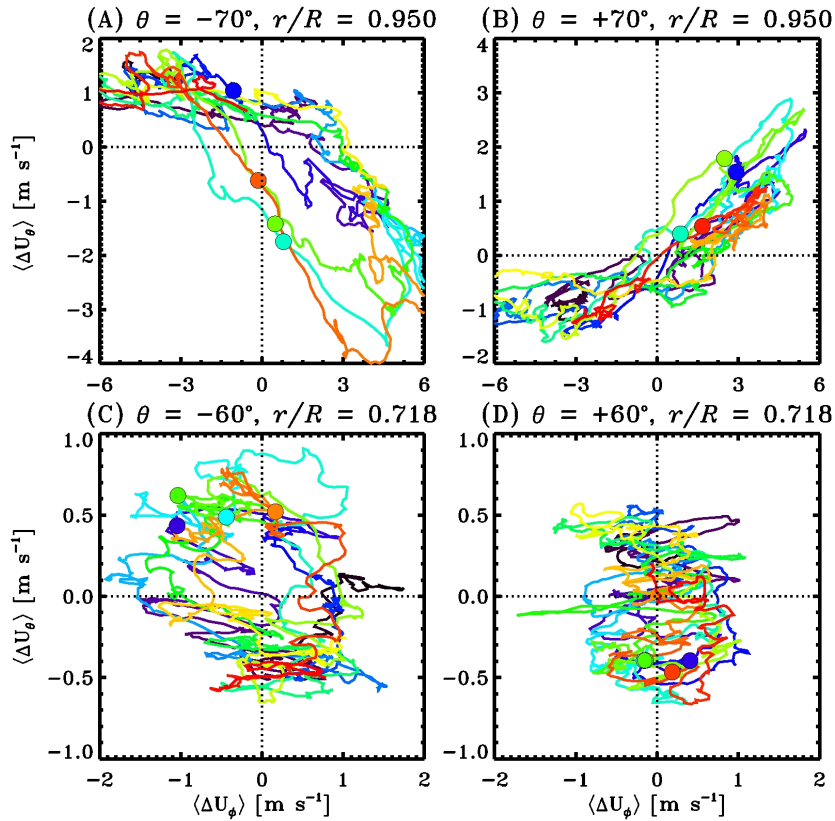


Figure 10. Phase diagrams of the perturbation in latitudinal velocity plotted vs. the perturbation in longitudinal velocity for two depths and four latitudes, as labeled above each panel. The color sequence indicates the temporal evolution : black - violet - blue - green - yellow - orange - red. The colored solid dots indicate the epochs of magnetic cycles maxima.

In the high latitude subsurface layers (panels A and B), both flow perturbations are strongly correlated in time, with the poleward latitudinal flow varying in phase with the prograde rotational acceleration. That local rotational acceleration (deceleration) should correlate in this manner to the variation of the latitudinal flow component, consistent with conservation of angular momentum in an axisymmetric fluid ring symmetrically contracting (stretching) as it gets displaced towards (away) from the rotation axis by the latitudinal flow. This suggests that, in this high-latitude location, the zonal dynamics are “enslaved” to the meridional flow dynamics. This situation does not hold everywhere, however, as evidenced by panels (C) and (D) of Fig. 10. These diagrams are now constructed from time series of zonal and latitudinal flow variations extracted at $\pm 60^\circ$ latitude at the core-envelope interface. The corresponding phase diagrams of zonal and latitudinal flow residuals are now markedly different from their high latitude subsurface counterparts on panels (A) and (B), with the two flow residuals now varying cyclically but out of phase with one another, with a phase lag $\sim \pi/2$. This indicates that the zonal dynamics cannot be reduced to angular momentum conservation in a contracting (expanding) fluid ring, and results from a more complex interplay of time-varying direct and indirect magnetically-mediated forcing (see also the companion analysis presented in Passos, Charbonneau, and Beaudoin, 2012).

3.4. Energetics of the torsional oscillations

The conclusion drawn above can be further substantiated through an analysis of the flux of energy to and from the various energy reservoirs defined by the flow and magnetic field. The evolution equation for the kinetic energy density of the flow, $\varepsilon_F = \bar{\rho}(\mathbf{u} \cdot \mathbf{u})/2$, takes here the form :

$$\frac{\partial \varepsilon_F}{\partial t} = -2\mathbf{u} \cdot \mathbf{F}_F + \mathbf{u} \cdot \mathbf{F}_B , \quad (24)$$

the volumetric force densities associated with the flow (\mathbf{F}_F) and magnetic field (\mathbf{F}_B) have been schematically grouped on the RHS. With $\mathbf{u} = d\mathbf{x}/dt$, both terms on the RHS correspond to the volumetric work done by the various forces on or against the flow \mathbf{u} . In what follows, we are interested in the energy flow in association with the torsional oscillations, so we will set $\mathbf{u} \equiv \mathbf{u}_\phi$, $\mathbf{F}_F \equiv F_{\text{Reyn}} + F_{\text{Circ}}$, and $\mathbf{F}_B \equiv F_{\text{Maxw}} + F_{\text{Magn}}$, as defined by Eqs. (16)–(19).

Figure 11 shows each power density contribution from Eq. (24) integrated over a conical volume going from the South pole to latitude -60° . Any negative contribution indicates energy extracted from the zonal flow. The only contribution that systematically does so here are the Reynolds stresses, moreover in a very well defined cyclic fashion. This is associated with the diffusive part of the Reynolds stresses acting to slow torsional oscillations, most importantly in the rising phase of the magnetic cycle, when the torsional oscillations are in their prograde acceleration phase. Energy injection is in fact dominated by the Coriolis force exerted on the meridional circulation, with peak energy transfer rate usually occurring in the first half of each magnetic half-cycle. Most remarkable perhaps is the fact that the magnetic forces (their amplitude being multiplied

by a factor of 5 on Fig. 11) mediate little or no significant *direct* transfer of energy to or from the mean zonal flow, and therefore that high-latitude torsional oscillations are not *directly* driven by the cycling large-scale magnetic field.

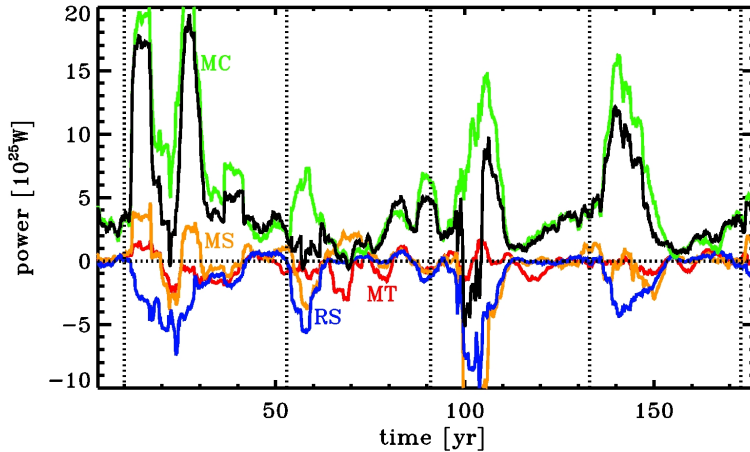


Figure 11. Temporal evolution of the power of various force contributions at the south pole of the sun, integrated for $-90^\circ < \theta < -60^\circ$. We represented the HD contributions multiplied by -2 to be consistent with Eq. (24). We also multiplied the magnetic components by 5 to enhance their temporal variations. Color coding as before : blue - Reynolds stresses; green - Coriolis force affecting the meridional flow; orange - Maxwell stresses; red - large-scale magnetic fields; black - total (variation of the energy in the flow in ϕ). The vertical dotted lines delineate subsequent magnetic half-cycles. All time series have been smoothed with a boxcar filter of width 5 yr

Table 1 lists the power densities associated with our zonal volumetric force components (left column), now integrated over the full 180 yr time span of the simulation segment. They are integrated spatially again over the Southern polar caps (middle column), as on Fig. 11, and over the full domain (right column). Once again, only the Coriolis force acting on the meridional flow injects energy in the zonal flow, but it surpasses by far all the other contributions. The magnetic force components, on average, extract energy from the zonal flow. This energy gets transferred to magnetic energy, which evolves according to

$$\frac{\partial \varepsilon_B}{\partial t} = -\nabla \cdot \mathbf{S} - \mathbf{u} \cdot \mathbf{F}_B , \quad (25)$$

where \mathbf{S} is the Poynting electromagnetic energy flux, and the second term on the RHS is the same as on the RHS of eq. (24), except of course for the sign. The inescapable conclusion is that direct magnetic driving of the torsional oscillations does not represent a saturation mechanism for the global dynamo operating in this simulation. However, we have seen previously that the magnetic cycle does drive large fluctuations in the meridional flow, and the Coriolis force acting on

Table 1. Mean powers obtained upon averaging in time the terms in Eq. (24) for two integration ranges. A positive value means an input in the flow energy.

Powers (W)	$-90^\circ < \theta < -60^\circ$	$-90^\circ < \theta < 90^\circ$
$-2 \int u_\phi F_{\text{Reyn}} dV$	-1.27×10^{25}	-2.84×10^{25}
$-2 \int u_\phi F_{\text{Circ}} dV$	$+5.35 \times 10^{25}$	$+1.26 \times 10^{26}$
$\int u_\phi F_{\text{Maxw}} dV$	-1.36×10^{24}	-1.57×10^{24}
$\int u_\phi F_{\text{Magn}} dV$	-6.47×10^{23}	-2.46×10^{24}

this cyclically forced flow is the main driver of torsional oscillations. Indeed, the energy analysis presented in §5 of Passos *et al.* (2012) indicates that magnetic driving of the latitudinal flow is the primary sink of magnetic energy in this simulation. The energy flow is thus of the form :

Magnetic energy \rightarrow meridional flow \rightarrow torsional oscillations \rightarrow small-scale turbulence \rightarrow (numerical) dissipation.

4. Concluding remarks

In this paper, we have carried out a focused analysis of one of the implicit large-eddy MHD simulation of solar convection computed by Ghizaru, Charbonneau, and Smolarkiewicz (2010) (see also Racine *et al.*, 2011; Charbonneau and Smolarkiewicz, 2012). To the best of our knowledge, these simulations remain unique in generating a spatially well-organized large-scale magnetic field component undergoing regular polarity reversals in a manner resembling in many ways the solar magnetic cycle. We have shown that a well-defined rotational torsional oscillation signal is present in the simulation, showing a surprisingly good degree of similarity with those observed in the sun, including: (1) frequency twice that of the magnetic cycle; (2) greater amplitudes in polar and subsurface regions, peaking at a few nHz; (3) peak prograde phase coinciding approximately with the peak in large-scale magnetic field; (4) diverging double-branch latitudinal structure; (5) depth-independent phase at most latitudes.

We investigated rotational dynamics by first computing from the simulation output the various contributions to angular momentum fluxes, in the MHD simulation as well as a parent, unmagnetized simulation otherwise operating under the same numerical and physical parameter settings. We could show that in the MHD simulation, the presence of a large-scale cycling magnetic field drives torsional oscillations not just directly through the associated large-scale magnetic torque, but also indirectly by modulating the other forces influencing zonal dynamics, most notably the transport of angular momentum by meridional flow. In fact, *all* force components driving the zonal flows undergo cyclic variations driven by the magnetic cycle, including the nominally “small-scale” Reynolds and Maxwell stresses.

We also examined the dynamical character of the rotational coupling between the convecting layers and underlying stably-stratified fluid layers. Because of the low-dissipative properties of the numerical scheme underlying the simulations, a tachocline-like shear layer builds up immediately beneath the nominal base of the convective layers, within which significant radial and latitudinal cyclically-varying fluxes of angular momentum develop. The net radial flux is determined by a competition between the meridional flow and Maxwell stresses within the tachocline ($0.7 \leq r/R \leq 0.718$) and by the magnetic torque and Maxwell stresses below. The latitudinal flux shows a strong cyclic signal, in phase with the magnetic cycle. It is dominated by the meridional flow within the tachocline, and by the large-scale magnetic torque below. The upper part of the stable layer is here an important player in setting the global cycle of angular momentum redistribution—and thus torsional oscillations—within the convection zone (on these issues see also Gilman, Morrow, and Deluca, 1989).

Turning to a simple analysis of the energetics of torsional oscillations, we could also show that the primary direct power source for torsional oscillations arising in the simulation is the action of the Coriolis force on large-scale meridional fluid motion, with Reynolds stresses acting to oppose these oscillations at most phases of the cycle. Surprisingly, direct driving by the large-scale magnetic torque makes only a minor contribution. This is in agreement with a parallel investigation by Passos, Charbonneau, and Beaudoin (2012), who carried out a similar energy analysis for the meridional flow and could show that magnetic driving of this flow represented the primary sink of magnetic energy. This suggests that saturation of global dynamo action in this simulation occurs through the magnetic driving of flows on large spatial scales, magnetic energy being first diverted into the meridional components, and subsequently, through angular momentum conservation, into torsional oscillations, where it eventually damps through turbulent stresses.

This state of affairs, should it carry over to the real Sun, has interesting consequences with regards to attempt to use fluctuations in large-scale flows as precursors to the solar cycle amplitude. More specifically, taken jointly with the results presented in Passos, Charbonneau, and Beaudoin (2012), our analysis suggests that fluctuations in the meridional flow may be better potential precursors than torsional oscillations, because the bulk of magnetic driving of large-scale flows occurs on and through this flow component. Re-analysis of extant surface Doppler measurements has now allowed to reconstruct variations of the surface latitudinal flow back to the beginning of cycle 22 (Ulrich, 2010; Dikpati *et al.*, 2010), and has shown that significant cycle-to-cycle variations indeed exist. We are currently pushing our simulations much further in time, as well as under different parameter regimes, which should allow a statistically sound investigation of the precursor potential of torsional oscillations as well as surface latitudinal flow.

This work was supported by Canada's Natural Sciences and Engineering Research Council, Research Chair Program, and by the Canadian Space Agency's Space Science Enhancement Program (grant # 9SCIGRA-21). PB is also supported in part through a graduate fellowship from the Université de Montréal's Physics department. The National Center for Atmospheric Research is supported by the National Science Foundation.

References

- Brown, B.P., Browning, M.K., Brun, A.S., Miesch, M.S., Toomre, J.: 2008, Rapidly Rotating Suns and Active Nests of Convection. *Astrophys. J.* **689**, 1354–1372. doi:10.1086/592397.
- Browning, M.K., Miesch, M.S., Brun, A.S., Toomre, J.: 2006, Dynamo Action in the Solar Convection Zone and Tachocline: Pumping and Organization of Toroidal Fields. *Astrophys. J. Lett.* **648**, 157–160. doi:10.1086/507869.
- Brun, A.S., Toomre, J.: 2002, Turbulent Convection under the Influence of Rotation: Sustaining a Strong Differential Rotation. *Astrophys. J.* **570**, 865–885. doi:10.1086/339228.
- Brun, A.S., Miesch, M.S., Toomre, J.: 2004, Global-Scale Turbulent Convection and Magnetic Dynamo Action in the Solar Envelope. *Astrophys. J.* **614**, 1073–1098. doi:10.1086/423835.
- Charbonneau, P., Smolarkiewicz, P.K.: 2012, EULAG-MHD: Simulation of the Global Solar Dynamo. *Journal of Computational Physics*.
- Christensen-Dalsgaard, J.: 2002, Helioseismology. *Reviews of Modern Physics* **74**, 1073–1129. doi:10.1103/RevModPhys.74.1073.
- Dikpati, M., Gilman, P.A., de Toma, G., Ulrich, R.K.: 2010, Impact of changes in the Sun's conveyor-belt on recent solar cycles. *Geophys. Res. Lett.* **37**, 14107. doi:10.1029/2010GL044143.
- Fan, Y.: 2009, Modeling the Subsurface Evolution of Active-Region Flux Tubes. In: M. Dikpati, T. Arentoft, I. González Hernández, C. Lindsey, & F. Hill (ed.) *Solar-Stellar Dynamos as Revealed by Helio- and Asteroseismology: GONG 2008/SOHO 21, Astronomical Society of the Pacific Conference Series* **416**, 489.
- Ghizaru, M., Charbonneau, P., Smolarkiewicz, P.K.: 2010, Magnetic Cycles in Global Large-eddy Simulations of Solar Convection. *Astrophys. J. Lett.* **715**, 133–137. doi:10.1088/2041-8205/715/2/L133.
- Gilman, P.A., Morrow, C.A., Deluca, E.E.: 1989, Angular momentum transport and dynamo action in the sun - Implications of recent oscillation measurements. *Astrophys. J.* **338**, 528–537. doi:10.1086/167215.
- Hill, F., Howe, R., Komm, R., Christensen-Dalsgaard, J., Larson, T.P., Schou, J., Thompson, M.J.: 2011, Large-scale Zonal Flows During the Solar Minimum – Where Is Cycle 25? In: *AAS/Solar Physics Division Abstracts #42*, 1610.
- Howard, R., Labonte, B.J.: 1980, The sun is observed to be a torsional oscillator with a period of 11 years. *Astrophys. J. Lett.* **239**, 33–36. doi:10.1086/183286.
- Howe, R.: 2009, Solar Interior Rotation and its Variation. *Living Reviews in Solar Physics* **6**, 1.
- Käpylä, P.J., Korpi, M.J., Brandenburg, A., Mitra, D., Tavakol, R.: 2010, Convective dynamos in spherical wedge geometry. *Astronomische Nachrichten* **331**, 73. doi:10.1002/asna.200911252.
- Miesch, M.S., Brun, A.S., Toomre, J.: 2006, Solar Differential Rotation Influenced by Latitudinal Entropy Variations in the Tachocline. *Astrophys. J.* **641**, 618–625. doi:10.1086/499621.
- Mitchell, W.M.: 1916, The history of the discovery of the solar spots. *Popular Astronomy* **24**, 562.
- Passos, D., Charbonneau, P., Beaudoin, P.: 2012, An exploration of non-kinematic effects in flux transport dynamos. *Solar Phys.*
- Prusa, J.M., Smolarkiewicz, P.K., Wyszogrodzki, A.A.: 2007, EULAG, a Computational Model for Multiscale Flows. *Computers & Fluids*. doi:10.1016/j.compfluid.2007.12.001.
- Racine, É., Charbonneau, P., Ghizaru, M., Bouchat, A., Smolarkiewicz, P.K.: 2011, On the Mode of Dynamo Action in a Global Large-eddy Simulation of Solar Convection. *Astrophys. J.* **735**, 46. doi:10.1088/0004-637X/735/1/46.
- Schuessler, M.: 1981, The solar torsional oscillation and dynamo models of the solar cycle. *Astron. Astrophys.* **94**, L17.
- Ulrich, R.K.: 2010, Solar Meridional Circulation from Doppler Shifts of the Fe I Line at 5250 Å as Measured by the 150-foot Solar Tower Telescope at the Mt. Wilson Observatory. *Astrophys. J.* **725**, 658–669. doi:10.1088/0004-637X/725/1/658.
- Yoshimura, H.: 1981, Solar cycle Lorentz force waves and the torsional oscillations of the sun. *Astrophys. J.* **247**, 1102–1112. doi:10.1086/159120.